Chapter 5

MUON PHASE ROTATION CHANNEL

Contents

5.1 Introduction

The basic concept is to collect as large an amount of pions as possible, channel them along a decay channel while using acceleration cells to collect as many particles as possible within a usable energy spread. The general strategy is to boost low-energy particles and decelerate higher energy particles by means of appropriately place acceleration cavities.

Two alternatives for the capture and phase rotation of pions issuing from the target and their muon decay products are being considered: namely an rf approach and an induction approach.

The rf approach is characterized by requiring that the rf cavities be placed close to the pion production target (i.e. within a few meters) in order that the frequencies for phase rotation be high enough that the cavities not become unreasonable in size. The induction linac approach is characterized by requiring a significant drift between the production target and the first induction cell (i.e. of the order of 25 m) in order to match the beam pulse length to acceleration wave lengths that can be reasonably achieved without incurring excessive core losses (i.e. 50 to 100 ns). The output muon pulse from the induction linac then needs to be compressed to $\sim$ 20 ns for injection into the cooling channel whereas the output pulse length of the rf approach to phase rotation is roughly matched to the cooling channel. Since the induction cells produce a factor of two or more lower accelerating gradient than the rf cells, the induction approach requires more axial length. On the other hand there are uncertainties about operating rf cavities in the high radiation environment within a few meters of the pion production target so discussion of both approaches is presented.

5.2 rf Approach

5.2.1 Introduction

The design of the phase rotation system is greatly influenced by the energy range chosen for the particle collection. We develop two solutions to accommodate a low-energy collection (50-250 MeV) and a high-energy collection (200-700 MeV). The pion production spectrum at the proton target is the most important factor in determining the best choice for the collection system.

The rf approach is characterized by designing a linac system which can begin immediately after the targeting of the main proton beam. We wish to begin the process as soon as possible so as to avoid the necessity of high-gradient, ultra-low frequency cavities. Figures 5.1 and 5.2 show the longitudinal structure of the beam after drift distances of 2 m and 24 m. Notice that lower frequency rf cavities are required for the cases in which either low-kinetic energy capture or long drifts are required.

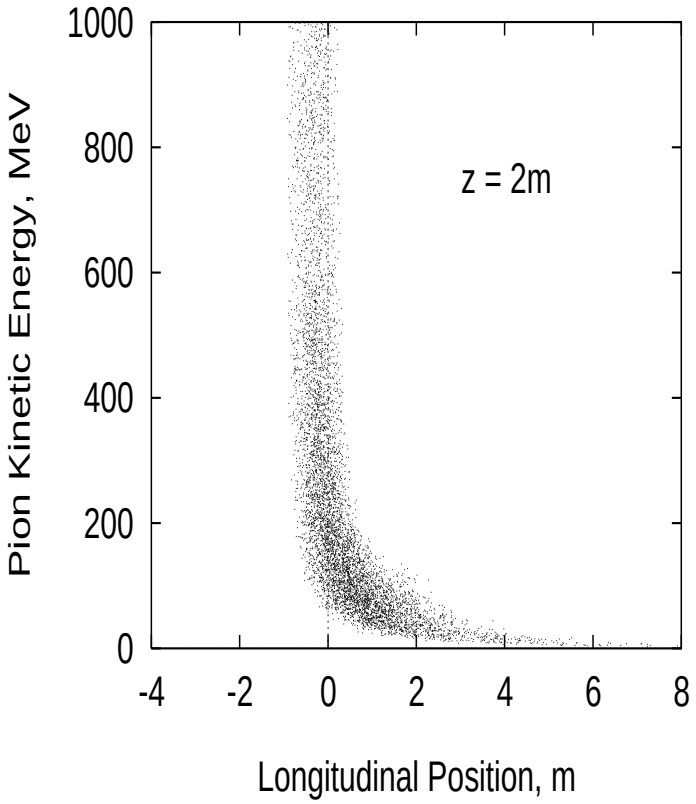

Figure 5.1: Collected particles after 2 m drift from the proton target

5.2.2 rf Cavities

The basic approach is to begin the phase rotation process as soon as possible in order to minimize the phase spread of the captured beam. By initiating the capture and phase rotation early we can take advantage of the higher accelerating gradients available with higher frequency cavities. Empirical evidence (see Figure 5.3) implies that pulsed rf systems in the frequency range below 500 MHz can be reliably operated at two Kilpatricks[1]. Also, the kinetic energy of the particles to be captured is of fundamental importance as it dictates the frequency of the cavities to be used. Notice that for particles with KE $>$ 200 MeV (See Figures 5.1 and 5.2), the phase spread of the particle beam is largely determined by the initial spread of the initiating proton beam (1 ns for this example).

Our choice of frequencies is determined by the phase spread of the beam. We begin with a high-frequency cavity which can deliver higher accelerating gradients and then proceed to lower frequency cavities as the beam continues it's longitudinal spread along the beam channel. Another important factor in choosing the rf cavity frequencies is the desire to have the same rf channel work for both positive and negative pulses. This can most easily be achieved by insuring that all cavities operate at an odd harmonic of some convenient fundamental frequency. Hence, for example, cavities of 300 MHz, 100MHz and 60 MHz

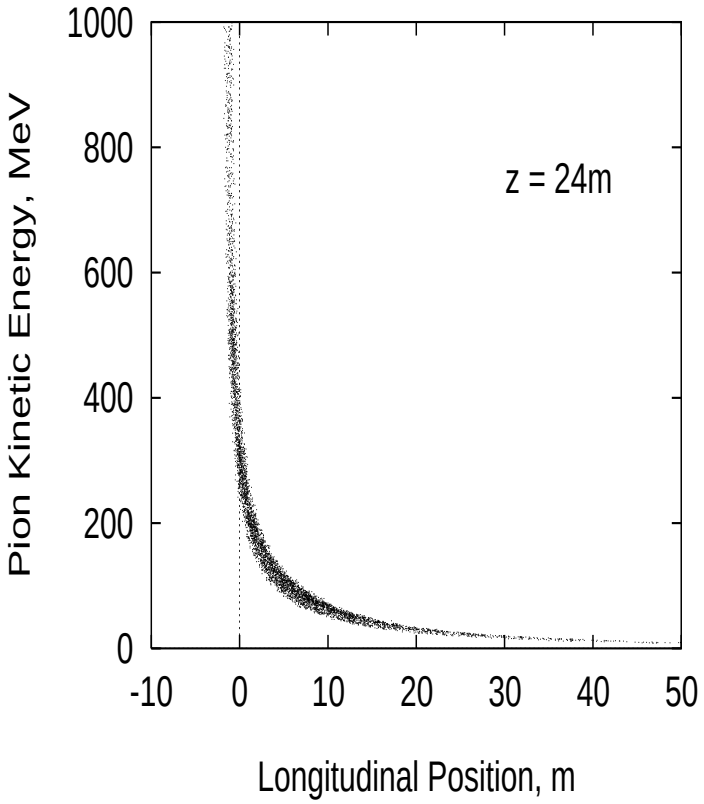

Figure 5.2: Collected particles after 24 m drift from the proton target

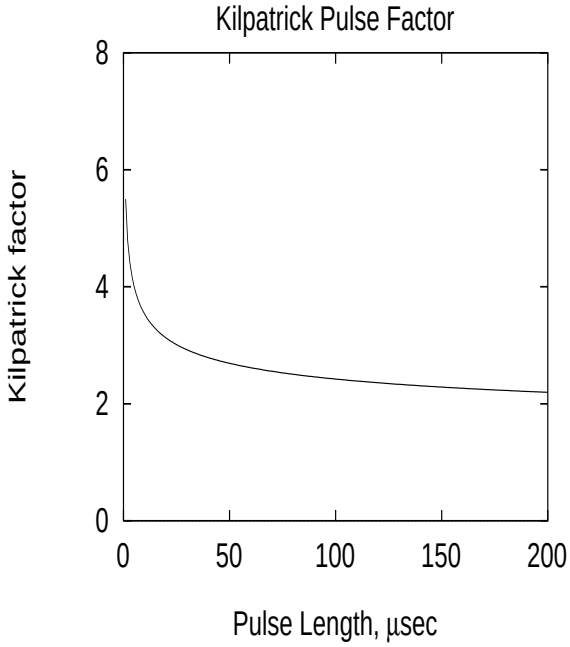

Figure 5.3: Kilpatrick Factor Limits for Pulsed rf Systems

(see Figure 5.4) satisfy this requirement since they are respectively 15×, 5×, and 3× the fundamental frequency of 20 MHz thus guaranteeing that a shift of 180 degrees at 20 MHz

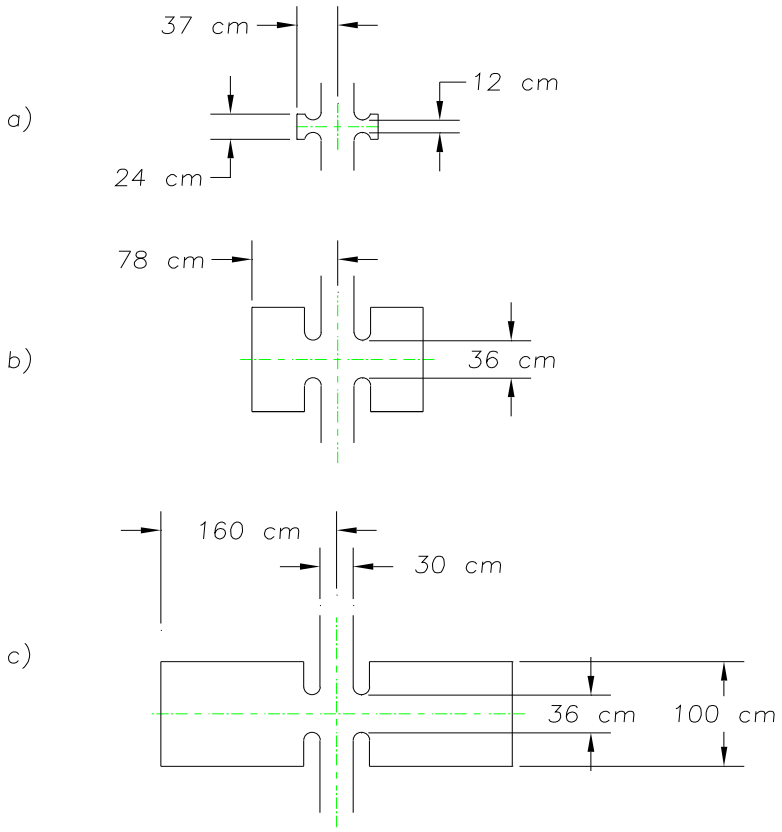

Figure 5.4: The high-energy collection rf cavities: a) 300 MHz; b) 100 MHz; c) 60 MHz. The fundamental harmonic is 20 MHz.

will result in a shift of an odd multipole of π for all frequencies.

We show in Figure 5.5, a scheme in which particles are collected and acceleration begun with the gap of the first cell placed 3 m beyond the beginning of the proton target. This solution for the high-energy collection starts with 300 MHz cavities and then proceeds down in frequency. For convenience of display, only three cavities of each frequency type is shown in Figure 5.5; however, the rf system parameters for the full solution are given in Tb.5.1. The average rf power is given assuming a 15 Hz repetition rate.

For low-energy collection (50 MeV-250 MeV) we need to consider lower frequency rf cavities. In this case we use a fundamental frequency of 10 MHz and choose 90 MHz, 50 MHz and 30 MHz cavities. Figure 5.6 shows a schematic of the rf cavities. The collection system is depicted in Figure 5.7 and the full rf system parameters are given in Tb.5.2.

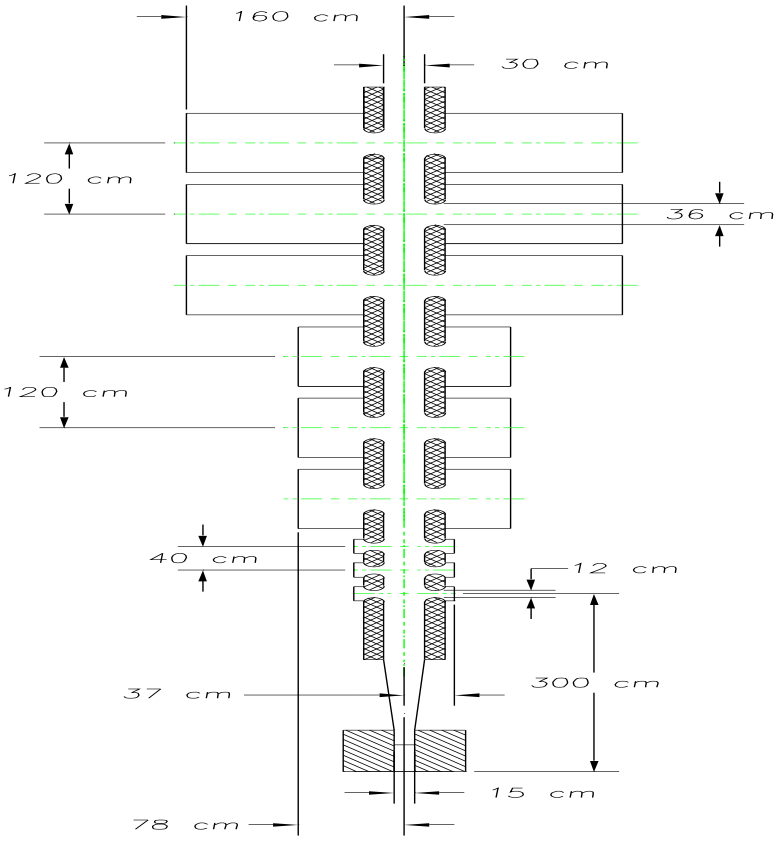

Figure 5.5: Schematic of the high-energy collection linac. Only three sections each are depicted of the 300, 100 and 60 MHz cavities. Hatched area is 20 T Bitter Solenoid, cross-hatched areas are 5 T superconducting solenoids.

5.2.3 Decay Channel Solenoids

The phase rotation magnet system is a continuation of the magnet system that captures and transports the pions that have been generated off the proton target. The solenoid field at the exit of the capture system must be continued in the phase rotation system. The pions in the phase rotation system still have a transverse momentum as high as 112 MeV/c. An induction of 5 T is required to contain the pion transverse momentum as the pions decay to muons as they are being bunched in the phase rotation system. Two approaches have been studied for the phase rotation rf cavity transport solenoid system. The first approach is to put the superconducting solenoids within the rf cavity so that they surround the cloud of pions coming from the target. The second approach surrounds the entire rf cavity with a large superconducting solenoid. In both cases the average magnetic induction along the channel that carries the pion cloud is 5 T. The channel that carries the pions to the phase

rotation system will have a warm bore diameter of 30 cm. The two approaches for the phase rotation rf cavity solenoids are illustrated in Figure 5.8 for rf cavities that have an outside diameter of 150 cm, a channel diameter of 30 cm and a cell length of 120 cm. In both cases, the acceleration gap is 36 cm.

Solenoids that are inside the rf cavity are less expensive, but the field must span the gap between the coils. If the superconducting solenoids are inside of the cavities, the gap between the coils is the cavity acceleration gap plus the allowance for the cryostat, the

Table 5.1: High-energy collection linac parameters

rf frequency [MHz]	300	100	60
Cavity Length [cm]	40	120	120
Full Gap length [cm]	12	36	36
Cavity Radius [cm]	37	78	160
Beam Pipe Aperture [cm]	30	30	30
Q/1000 (from SFISH)	21.5	54.8	44.6
Avg Gradient [MV/m]	12.5	4.5	3.6
rf Peak Power [MW]	8.8	2.2	1.1
Avg Power (15Hz) [KW]	10	19	13
Stored Energy [J]	101	166	208
Linac Segment [m]	12	12	54
Total Power (15Hz) [KW]	300	192	585

Table 5.2: Low-energy collection linac parameters

rf frequency [MHz]	90	50	30
Cavity Length [cm]	120	120	120
Full Gap length [cm]	36	36	36
Cavity Radius [cm]	90	206	126
Beam Pipe Aperture [cm]	30	30	30
Q/1000 (from SFISH)	53.4	71.1	16.8
Avg Gradient [MV/m]	4.2	3.3	2.1
rf Peak Power [MW]	1.8	1.1	4.8
Avg Power (15Hz) [KW]	17	26	43
Stored Energy [J]	165	261	423
Linac Segment [m]	6	18	18
Total Power (15Hz) [KW]	85	390	640

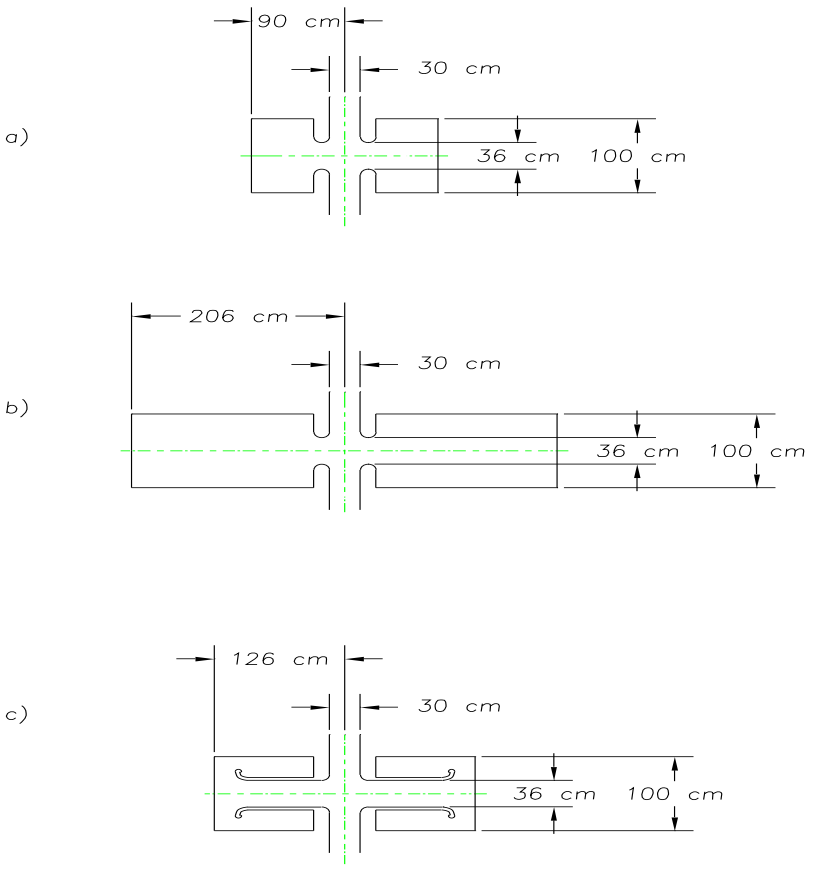

Figure 5.6: The low-energy collection rf cavities: a) 90 MHz; b) 50 MHz; c) 30 MHz. The fundamental harmonic is 10 MHz.

insulation and the end of the bobbin. The best that can reasonably be expected is a gap between coils that is only 4 cm larger than the accelerator gap. The gap between the coil ends shown in Figure 5.8a is about 40 cm. In addition, a 3 cm gap is shown in the middle of the superconducting coil. This gap allows the coil bobbin to be attached to the cryostat cold mass support system, which is not shown in Figure 5.8. The ends of the coils are built up to make up for the current that is lost in the gap. In order for there to be an average induction of 5 T, there must be 4.775 MA turns in each 120 cm long cell. The magnetic induction along the axis of the solenoid will not be uniform. The 3 cm gap in the middle of the coil has almost no effect on field uniformity, but the 40 cm gap between the coils will have a large effect on the field uniformity. The reason for the lack of field uniformity is that the 40 cm gap between the coils is larger than the inside diameter of the coils (about 34 cm). The 3 cm gap has only a small effect on the field uniformity because this gap is much smaller than the coil diameter. The effect of coil diameter and the gap between coils is shown in

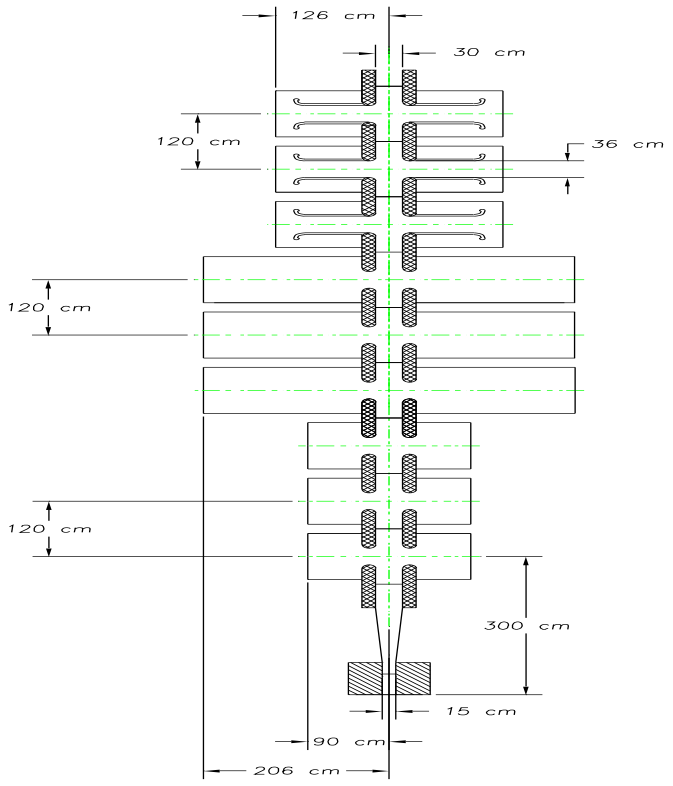

Figure 5.7: Schematic of the low-energy collection linac. Only three sections each are depicted of the 90, 50 and 30 MHz cavities. Hatched area is $20\,T$ Bitter Solenoid, cross-hatched areas are $5\,T$ superconducting solenoids.

Figure 5.9 and Tb.5.5.

We consider the possibility that the solenoidal axial field uniformity in the decay channel may have to be better than ± 5 % to avoid resonant particle losses. In order to improve the field uniformity, we have developed additional rf cavity solutions in which all cavities have axial lengths of 40 cm and accelerating gaps of 12 cm while retaining the 30 cm beam aperture for the decay channel. These rf solutions are given in Tbs.5.3 and 5.4.

The superconducting solenoid outside of the cavity is illustrated in Figure 5.8b. The gap between the coils in governed by the distance needed between coils to get services into the rf cavity. This gap will allow for a 10 cm warm diameter pipe to penetrate through the solenoid cryostat. If holes are provided for rf cavity services, the cryostat for the superconducting solenoid coils can be made quite long (say eight or ten rf cavity modules long). The current density in the larger diameter coils must be lower because the magnet stored energy is higher.

As a result, the coils are shown to be thicker. The field uniformity along the magnet axis is much better for the solenoids located outside the rf cavity compared to the solenoids located inside the rf cavity. The gap between the coils for the large coil case is small compared to the solenoid diameter. The effect of the solenoid diameter on field uniformity and other parameters is shown in Figure 5.9 and Tb.5.5.

From Figure 5.9 and Tb.5.5, it is clear that cases 1 and 2 with the coil inside the cavity have a far less uniform field along the axis than does case 3 where the solenoid is outside the rf

Table 5.3: High-energy collection linac parameters

rf frequency [MHz]	300	100	60
Cavity Length [cm]	40	40	40
Full Gap length [cm]	12	12	12
Cavity Radius [cm]	37	87	87
Beam Pipe Aperture [cm]	30	30	30
Q/1000 (from SFISH)	21.5	33.5	14.4
Avg Gradient [MV/m]	12.5	4.5	3.6
rf Peak Power [MW]	8.8	1.0	3.4
Avg Power (15Hz) [KW]	10	5	13
Stored Energy [J]	101	53	131
Linac Segment [m]	12	12	54
Total Power (15Hz) [KW]	300	158	1760

Table 5.4: Low-energy collection linac parameters

rf frequency [MHz]	90	50	30
Cavity Length [cm]	40	40	40
Full Gap length [cm]	12	12	12
Cavity Radius [cm]	100	98	140
Beam Pipe Aperture [cm]	30	30	30
Q/1000 (from SFISH)	34.3	13.5	11.1
Avg Gradient [MV/m]	4.2	3.3	2.1
rf Peak Power [MW]	0.9	3.5	2.5
Avg Power (15Hz) [KW]	5	15	14
Stored Energy [J]	52	149	145
Linac Segment [m]	6	18	18
Total Power (15Hz) [KW]	78	670	652

Table 5.5: Parameters for three solenoid magnet configurations in or around a 150 cm outside diameter rf cavity

Parameter	CASE 1	CASE 2	CASE 3
rf Cell Length (cm)	120	120	120
Cavity Outside Diameter (cm)	150	150	150
Solenoid Coil Inside Diameter (cm)	34	34	160
Solenoid Coil Outside Diameter (cm)	44	44	180
Cavity Acceleration Gap (cm)	36	11	36
Gap Between the Coils (cm)	40	15	15
Coil Length per Cell (cm)	80	105	105
Average Induction along Axis (T)	5.00	5.00	5.00
Minimum Induction on Axis, B_{min} (T)	2.324	4.381	4.986
Maximum Induction on Axis, B_{max} (T)	6.520	5.276	5.103
Induction Ratio B_{max}/B_{min}	2.80	1.20	1.02
Pion Chamber Diameter (cm)	44	32	30
Peak Induction in the Coil (T)	7.24	5.82	5.31
Stored Energy (MJ per meter)	1.35	1.14	21.2

cavity. Reducing the acceleration gap improves the field uniformity along the axis (compare cases 1 and 2), but the price for increased field uniformity on the axis is an increased length of the phase rotation system.

A non-uniform solenoid field along the axis of the phase rotation linac has two consequences. First the diameter of the pion decay channel must be increased to accommodate the transverse momentum in the pions at the lowest field along the axis. Second a periodic field may induce oscillations in the beam that could lead to pion losses. The increase in beam radius due to the induction decrease on axis may be estimated using the following expression:

$$r\left(z\right) = \sqrt{\frac{B_{ave}}{\mathrm{B\left(z\right)}}}\; r\left(B_{ave}\right) \tag{5.1}$$

where r(z) is the radius of the beam pipe at location z and B(z) is the magnetic induction at the location z. r(B_{ave}) is the radius of the beam pipe when the induction is at the average induction B_{ave}. For a transverse momentum of 112 MeV/c, B_{ave} = 5 T and r(B_{ave}) = 15 cm.

From Tb.5.5, one can see that the peak induction in the winding is considerably higher than the average induction for the cases 1 and 2 where the solenoid is inside the cavity. This

increase in magnetic induction affects the performance of the superconductor.

The stored energy per unit length for solenoids surrounding the cavity is much larger than for the case when the solenoids are inside the cavity. The cost of the superconducting solenoid is proportional to the stored energy to some power (from 0.6 to 0.7). From a cost standpoint, it can be argued that decreasing the field on the solenoid axis is desirable, but the diameter of the beam tube must be increased in order to contain a pion beam with the desired transverse momentum.

When the superconducting solenoids are installed outside the rf cavities, the cavity design should minimize the cavity diameter and the solenoid coils should be as close to the cavity as possible. The gaps between solenoid coils are far less important than when the coil is outside the cavity, but these gaps should be minimized to improve field uniformity.

5.2.4 Beam Dynamics

The beam dynamics of the particle collection system is modeled with the computer program PARMELA. Particle are generated within a target surrounded by a high-field solenoid (20 to 28 T are considered) and subsequently transported down a lower field solenoid (5 to 7 T) channel with rf cavities placed at appropriate intervals. Rf phases are adjusted for each cell to optimize the longitudinal phase of the particle bunch exiting the complete system. Figure 5.10 shows the results of capturing and phase rotating particles for two collection systems corresponding to the collection regions described earlier. The final number of particles collected for each system is dependent on the assumed initial particle spectra.

5.3 Induction Linac Approach

5.3.1 Introduction

In this section we describe an induction linac approach to phase rotation of the muon bunch prior to entering the cooling channel. The instantaneous energy spread is reduced from $\frac{dE}{E} \approx \pm 100\,\%$ to $< \pm 10\,\%$ by allowing the muons to drift and spread longitudinally and then using induction cells to phase rotate the beam. The head-to-tail sweep can be reduced from an energy spread of $\approx 200\,\%$ to a few per cent. The equations describing longitudinal pulse dynamics, voltage waveforms and induction cell parameters have been given in a previous report[2]. That report applied the equations to a muon production spectrum from early considerations of the muon collider which had high collection energy (0.3 to 1.0 GeV). Results for the decay of muons from low-energy captured pions have been examined. Specifically

we consider two cases: (1) $0.15 < E_\mu < 0.3\,\mathrm{GeV}$ and $0.25 < E_\mu < 0.7\,\mathrm{GeV}$. In this section muon energy is total energy including the muon rest mass since that is what appears in the dynamical equations.

5.3.2 Input Muon Pulse Energy and Intensity

A typical distribution of mean energy and beam current in a muon pulse is shown in Figures 5.11. This case corresponds to the lower energy of the two cases we consider here. The time behavior of energy and current are well characterized by simple exponential functions given in the caption to Figures 5.11. We refer to the Proton Source and Targetry and Pion Production chapters for detailed discussion of pion production, capture and decay into muons. The calculations in Figures 5.11 were done with 24 GeV/c protons incident on a Hg target, 5×10^{13} protons per pulse, rms pulse width 3 ns. The Hg target is in a 20 T solenoid field, tapering to 5 T in the pion decay channel. The spectra in Figures 5.11 are 24 m from the target and the integrated yield from 0 to 50 ns is approximately 0.4 muons per incident proton. Because of the exponential attenuation it is relatively inefficient to accelerate the lowest energy muons. We will somewhat arbitrarily truncate the muon distribution at 50 ns. There is also a high energy group of muons with energy extending above 1 GeV and arriving in time bins before T = 0 in Figures 5.11. These highest energy muons have a high instantaneous energy spread $\frac{dE}{E} \approx 0.5$ and are less amenable to phase rotation. They will also be truncated. Some of these muons are treated in the higher energy case with phase rotation beginning at z = 171 m instead of 24 m. The instantaneous rms energy width of muons from 0 to 50 ns is shown in Figure 5.12 and falls from $\frac{dE}{E} = 0.08$ at the head to $\frac{dE}{E} = 0.02$ at the tail.

The Monte Carlo calculations for the high-energy case, $0.25 < E_\mu < 0.7\,\mathrm{GeV}$, can also be fit with simple exponential functions. At z = 171 m from the proton target $\mathrm{E(GeV)} = 0.213 + 0.516\,e^{-\mathrm{T(ns)}/25.9}$ and $\mathrm{I(A)} = 87\,e^{-\mathrm{T(ns)}/41.1}$. For phase rotation we will consider the pulse extending from 0 to 70 ns. The integrated yield from 0 to 70 ns is approximately 0.4 muons per incident proton.

5.3.3 Acceleration Wave Shape, Voltage Gradient and Mean Muon Energy

The time dependence of acceleration wave shapes and the resultant flattening of mean energy as the muons propagate through the accelerator are shown in Figures 5.13. The rate of spreading of the wave shape depends on the energy distribution, transverse momentum

distribution and accelerating gradient. The initial energy distribution in Figure 5.13b at z = 0 is the same as Figure 5.11a. The mean transverse momentum is 25 MeV/c and the rms transverse momentum width is 43 MeV/c. The acceleration wave shapes shown in Figure 5.13a produce a flat energy profile at z = 170 m, which is simply the initial head-to-tail energy spread divided by the average accelerating gradient that is applied to the tail of the pulse, here assumed to be 1 MV/m. The pulse width of the flat distribution at z = 170 m is 130 ns. The gradient in an induction accelerator is ultimately limited by the increasing radial size of the magnetic cores and of course also by the fraction of accelerator length that can be occupied by induction cells. Assuming 40 % of the axial accelerator length is available for induction cells a gradient of 1 MV/m seems to be practical and is well below the theoretical maximum.[2] A factor of two increase in gradient and reduction in axial length may be possible. The higher energy case is qualitatively similar to Figures 5.13 but the overall accelerator length is 480 m due to the larger initial head to tail energy spread. The accelerating gradient is again taken to be 1 MV/m. Parameters for both cases will be summarized in the following section.

The width of the output muon pulse from the phase rotation induction linac needs to be reduced from $\sim$ 130 ns to $\sim$ 20 ns before injection into the muon cooling channel. This can be accomplished by continuing the acceleration until the energy of the tail slightly exceeds the head (i.e. $\sim$ 10%) and then allowing the bunch to ballistically compress as it drifts. The drift distance and fractional muon loss due to decay are decreased if the compression is carried out at low energy. This could be done by decelerating the muons once the phase rotation is accomplished. Alternatively, the phase rotation could be done by simultaneously decelerating the head and accelerating the tail of the pulse so the output energy matches what is desired for compression. The optimum induction accelerator strategy for matching to the cooling channel is a subject for further study.

5.3.4 Accelerator Parameters

A schematic of an induction cell is shown in Figure 5.14 which also defines some of the geometric quantities that appear in Tb.5.6. There are four components to the cell: (1) the high voltage pulsed power feed, (2) the magnetic core, (3) the vacuum insulator and (4) the acceleration gap. The induction core has axial length w and radial width ΔR. The inside and outside radii of the magnetic core are R_1 and R_2. The high voltage pulsed power lead enters along one side of the core, encircles it and returns to ground. The magnetic core volume behind the vacuum insulator is filled with insulating dielectric fluid. There are three insulating gap widths indicated: the dielectric gap g_d, the vacuum insulator gap g_s and

the acceleration gap g_v. These must withstand dielectric breakdown, vacuum surface flash over and vacuum breakdown respectively. The angle between the insulator surface and the metal electrode surfaces on the vacuum side is shown to be $\approx 25^\circ$ to 45° to maximize the breakdown limiting field strength. The re-entrant acceleration gap prevents radiation from the beam channel reaching the insulator surface and possibly initiating breakdown. The primary concern is shielding the synchrotron radiation produced by muons and by electrons from muon decay. The total length of the induction cell is L_c. The values of these geometrical parameters as well as certain electrical parameters for the two cases we are considering are given in Tb.5.6.

The entire accelerator consists of axially stacked arrays of acceleration cells as in Figure 5.14 interleaved with 5 T superconducting solenoids for focusing the beam. The inside and outside radii of the solenoid cryostats are assumed to be 15 and 30 cm respectively. The inside radius coincides with the beam tube radius. For the examples in Tb.5.6 we have assumed that the solenoids occupy 60 % of the axial length and the acceleration cells 40 %. The inside radius of the magnetic induction core is assumed to be $R_1 = 30\,\mathrm{cm}$. Increased accelerating gradient could be achieved by increasing the inner magnetic core radius and allowing the core volume to extend over the outside of the solenoids. The integrated design of the acceleration cells and solenoids must avoid saturation of a significant fraction of the induction core by solenoid flux leaking out of the beam channel. The cell voltage $V_0 = 50\,\mathrm{kV}$ was chosen with consideration of how the pulse power system might be configured. In principle one could choose spark gaps, thyratrons or saturating magnetic cores for the final stage switch into the induction cores since they can all be configured to handle the required power level. Spark gaps could allow operation up to $V_0 = 250\,\mathrm{kV}$. However electrode erosion would require replacement after a few million pulses, or a day of operation at 30 Hz, so they are ruled out. Saturating magnetic cores have been shown to switch coaxial lines charged up to $\approx 200\,\mathrm{kV}$ at kHz rep rates and high power thyratrons are commercially available for switching up to $\approx 50\,\mathrm{kV}$ so either of these seems possible. 50 kV was chosen as a compromise between these two possibilities; a saturating magnetic core discharging a coaxial line charged to $2V_0 = 100\,\mathrm{kV}$ or a thyratron discharging a Blumlein line charged to $V_0 = 50\,\mathrm{kV}$. Induction linac parameters for the two cases (1) $0.15 < E_\mu < 0.3\,\mathrm{GeV}$ and $0.25 < E_\mu < 0.7\,\mathrm{GeV}$ are given in Tb.5.6. They are determined by four primary relationships for; (1) the cell axial length, (2) the volt-seconds of the magnetic core, (3) the voltage rise time and (4) the voltage insulation and shielding of the vacuum insulator.[2] For the magnetic core material we have chosen *Metglas 2605SC* which has high saturation magnetic flux and the dynamic hysteresis loss has been measured in the switching times of interest.[3, 4] We assume a packing fraction $p_f = 0.75$. Reasonable allowances and considerations have also been made for mechanical

structure, voltage insulation and induction core cooling. Where it makes a difference, parameters given in Tb.5.6 are for the last cell in the accelerator which has the highest volt seconds requirement. Values for the entire accelerator are then obtaining by multiplying values for the last cell by the number of cells and ignoring the $\approx 20\,\%$ corrections that arise if axial averages are taken.

The overriding difference between the two cases in Tb.5.6 is the factor of 2.8 in axial length due to the head to tail energy spread at z = 0 and assumed accelerating gradient V'_m = 1 MV/m in both cases. The acceleration cells for the two cases are rather similar and the differences in detail are traceable to the somewhat different acceleration wave shapes imposed by the two muon energy spectra. Each cell consumes about 38 J of electrical energy per pulse, or at 30 Hz rep rate (2 pulses at 15 Hz to accommodate each muon charge state) about 1.1 kW of electrical power. The electrical energy is about evenly divided amongst hysteresis loss (39 %), charging the cell capacitance (25 %) and reflected energy due to impedance mismatch (36 %). The magnetic core leakage current is 3.6 to 4 kA so beam loading with a maximum current ≈ 100 A is relatively light and produces negligible pulse distortion. Overall the first case consumes 4.1 MW of pulsed electrical power and the second case 12 MW. The total weight of *Metglas 2605SC* is 104 tonne for the first case and 229 tonne for the second. To get a feeling for the scale of induction accelerator involved, the total weight of magnetic core material involved is ten to twenty times less than has been contemplated for the drive beam of a relativistic klystron version of a 1 TeV e^+e^- collider.[5]

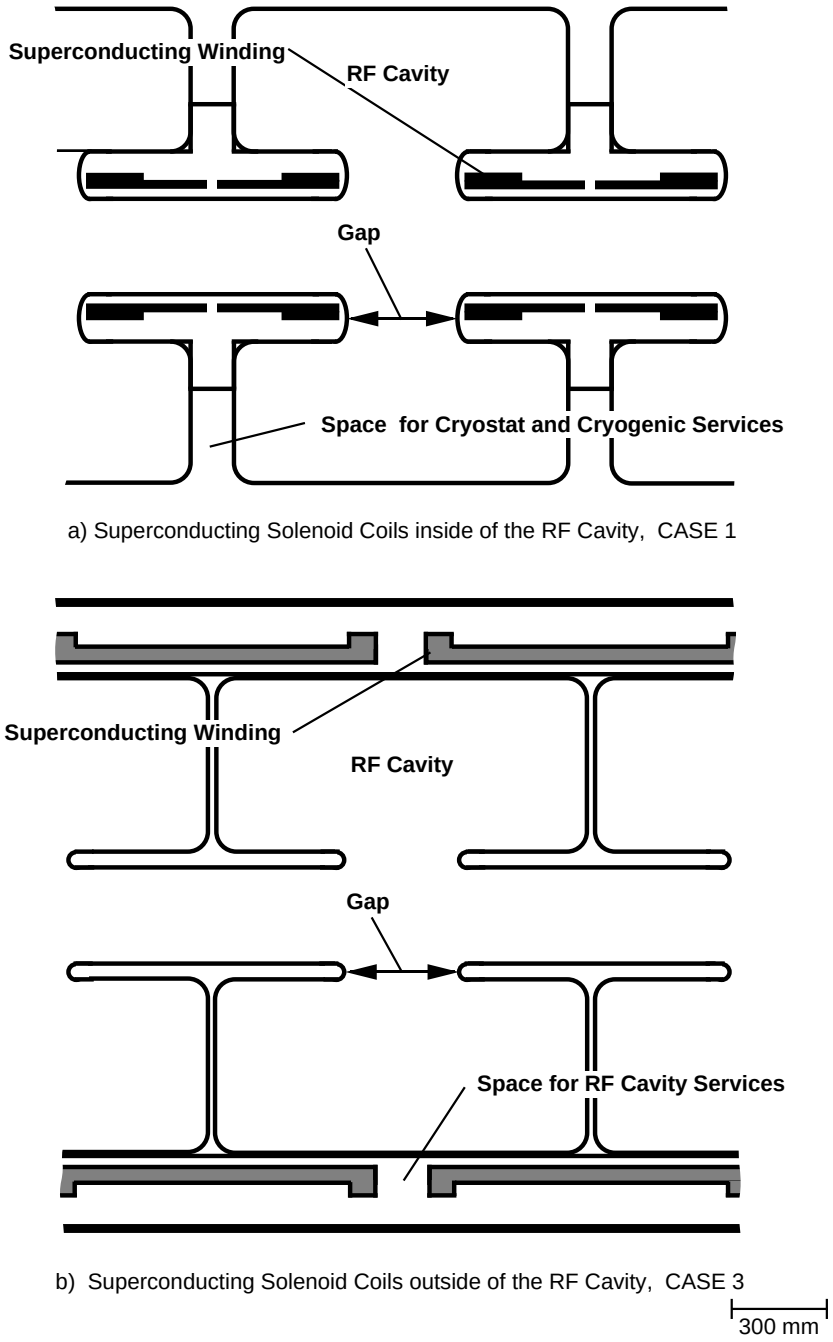

Figure 5.8: A schematic representation of superconducting solenoid scenarios for the phase rotation cavities

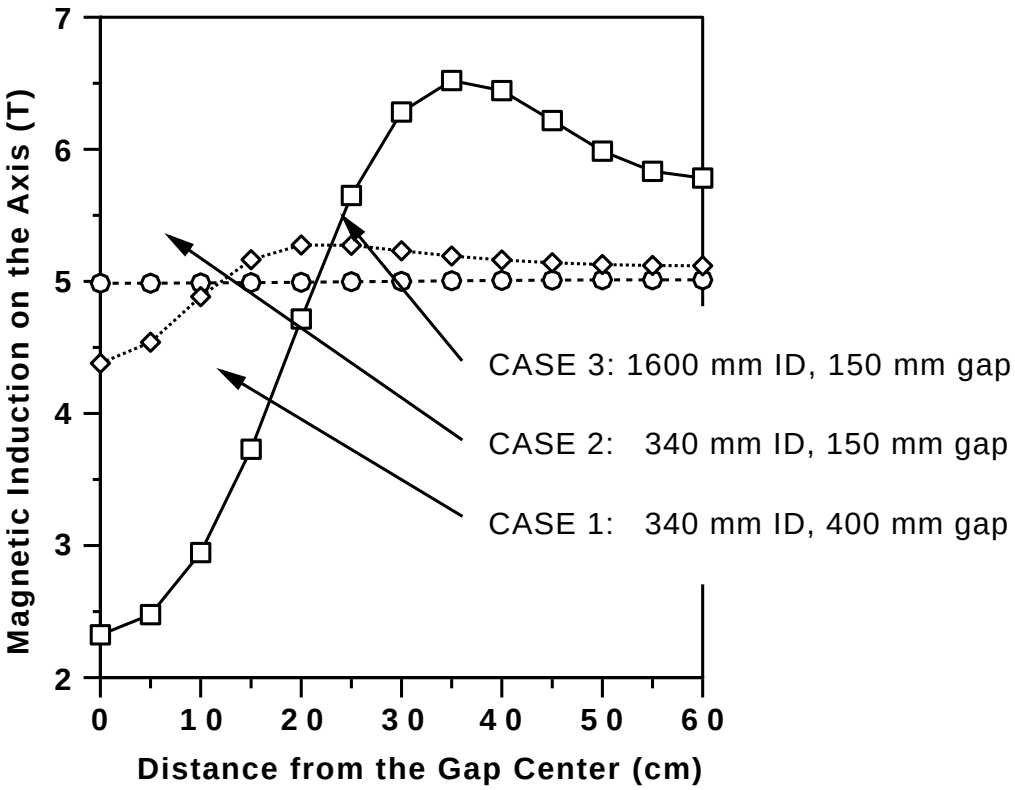

Figure 5.9: Magnetic induction along the rf cavity axis for three solenoid magnet and rf cavity configurations

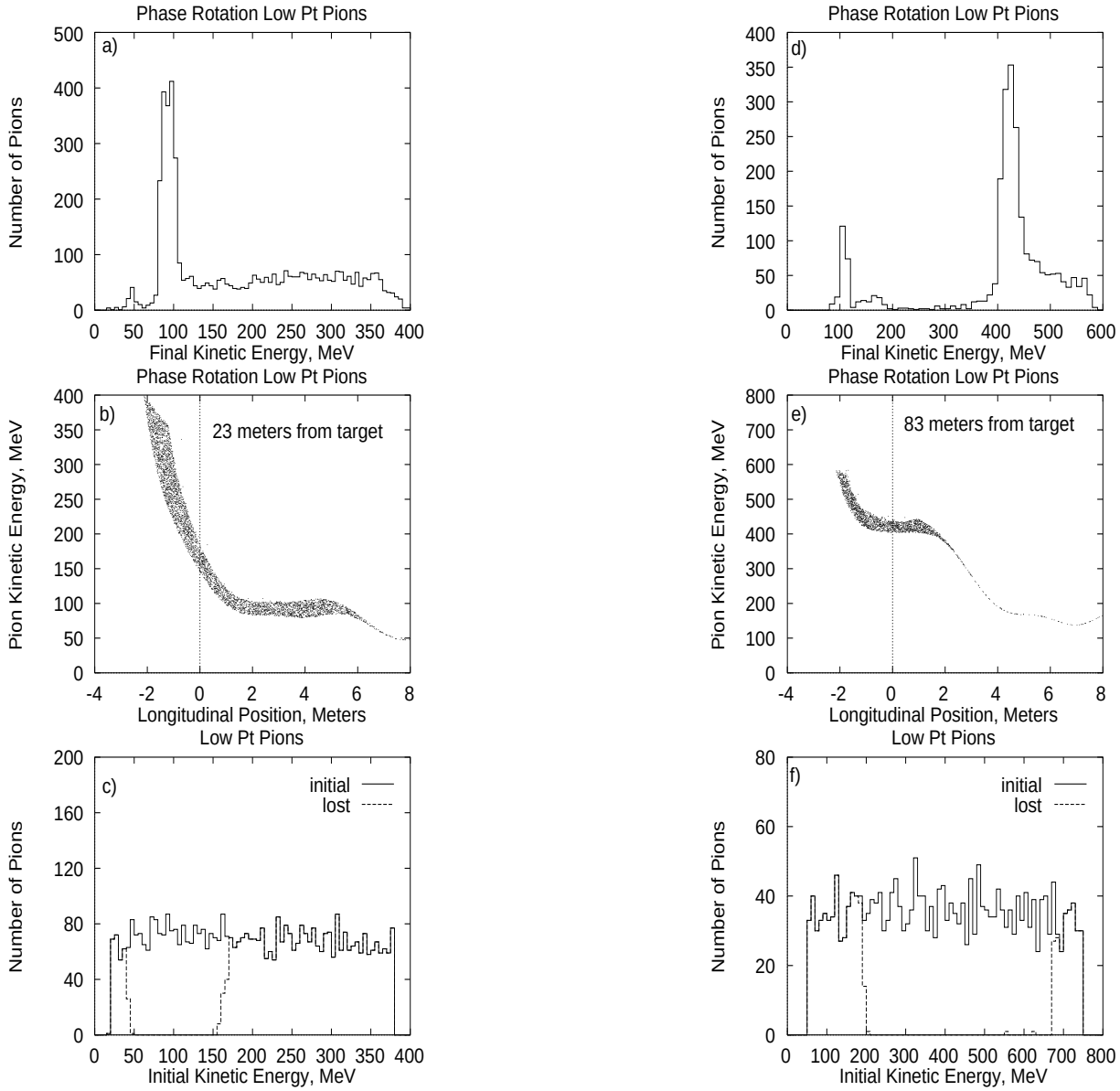

Figure 5.10: The results of particle dynamics modeling of pion capture immediately following the proton target. a), b), and c) depict results in which low-kinetic energy pions are collected, while d), e) and f) depict the corresponding results for the high-kinetic energy case.

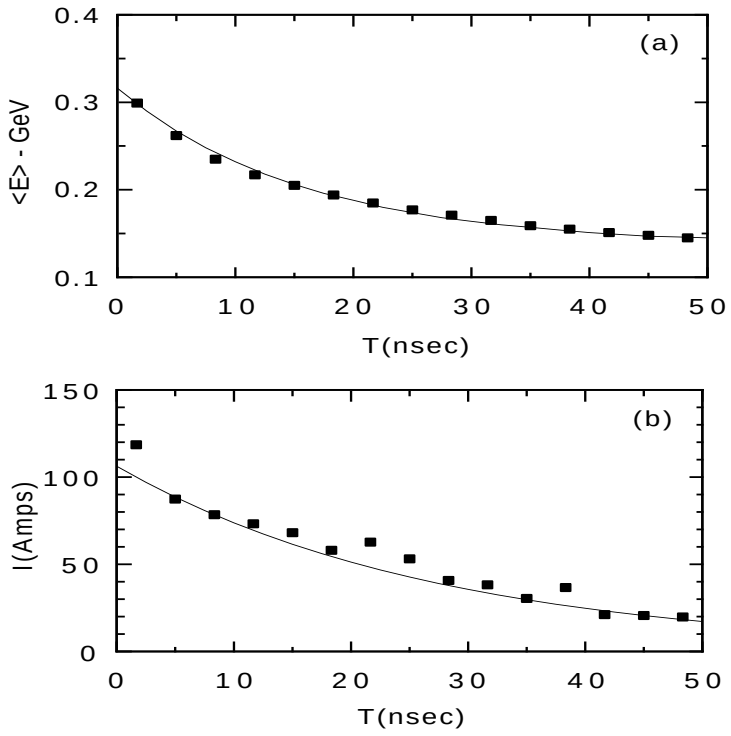

Figure 5.11: (a) Mean muon energy and (b) muon current z = 24 m from the production target. Solid square symbols are Monte Carlo results, the solid lines are exponential fits; $\mathrm{E(GeV)} = 0.137 + 0.179\, e^{-\mathrm{T(ns)}/15.8}$ and $\mathrm{I(A)} = 106.2\, e^{-\mathrm{T(ns)}/27.5}$.

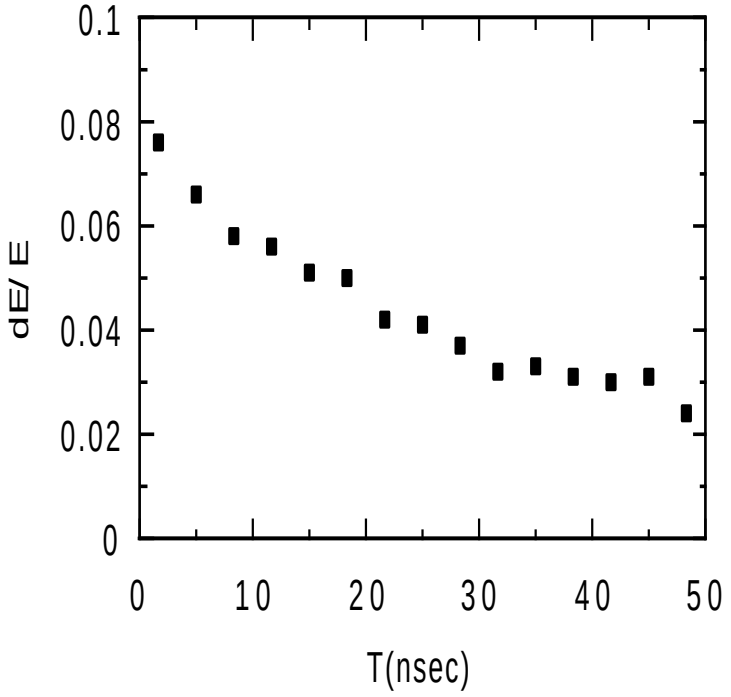

Figure 5.12: Instantaneous rms energy width of muons z = 24 m from the target.

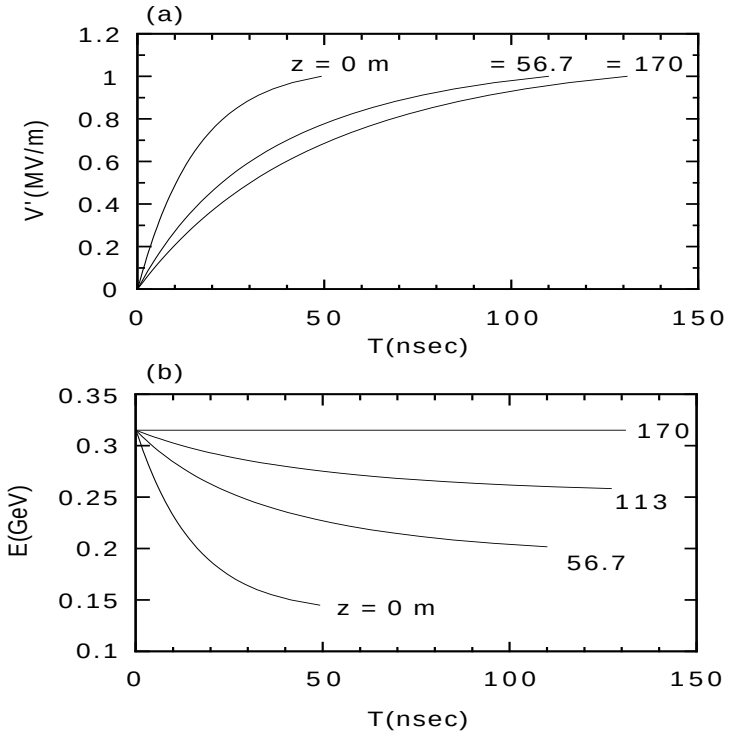

Figure 5.13: (a) Accelerator gap voltage wave shape at z = 0, 56.7 and 170 m and (b) mean muon energy at z = 0, 56.7, 113 and 170 m. z = 0 is 24 m from the production target.

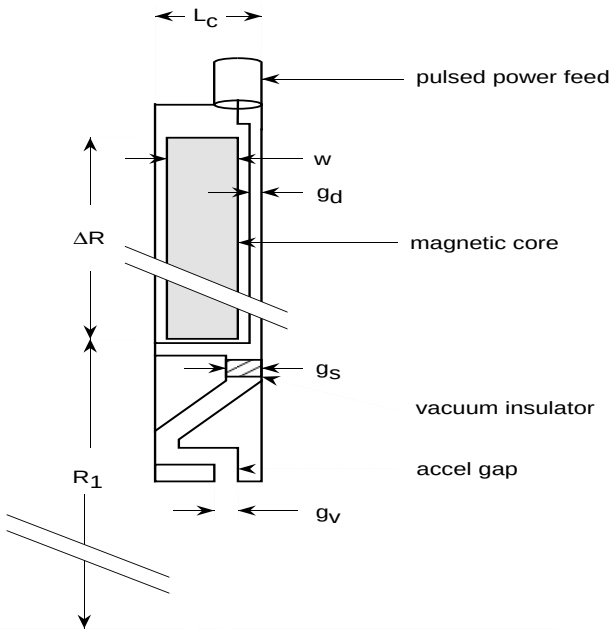

Figure 5.14: A schematic of an induction acceleration cell.

Table 5.6: Induction accelerator parameters for two cases; (a) input muon spectrum 0.145 to 0.316 GeV and (b) 0.244 to 0.720 GeV.

Parameter	Units	Value	
		(1)	(2)
Voltage gradient, V′	MV/m	1	
Cell voltage, V	kV	50	
Cell length, Lc	cm	1.88	1.85
E_{min}	GeV	.145	.244
E_{max}	GeV	.316	0.720
Accel length	m	171	476
Number of cells		3642	10302
Cell voltage rise time	ns	46.8	44.1
Pulse length	ns	131	114
Volt seconds per cell	$10^{-3}V \times s$	4.35	3.65
Rep rate	Hz	30	
Maximum core flux swing	T	2.5	
Average Bdot	$T/\mu s$	19.1	22.0
Core loss	kJ/m^3	3.77	4.34
Core axial width, w	cm	1.34	1.38
Inside radius of magnetic cores, R_1	m	0.30	
Core outer radius, R_2	m	0.462	0.428
Dielectric gap width, g_d	mm	2.73	1.89
Dielectric gap field stress	MV/cm	0.183	0.264
Vacuum insulator width, g_s	cm	1.0	
Accel gap width, g_v		0.5	
Vacuum insulator field stress limit	kV/cm	50	
Accel gap field stress limit	kV/cm	100	
Dielectric gap field stress limit	MV/cm	0.5	0.55
Insulator shielding margin	mm	1.11	0.717
Cell capacitance	nF	8.56	9.30
Core leakage resistance	Ohms	8.60	7.34
Core leakage current	kA	3.61	3.97
Vol. of core matl.(2605SC) per cell	$10^{-3}m^3$	3.90	3.03
Core weight per cell	kgm	28.5	22.2

Parameter	Units	Value		
		(1)		(2)
Core energy loss per cell per pulse	J	14.7		13.2
Gap capacitance energy per cell per pulse	J		9.43	9.93
Mismatch energy per cell per pulse	J	13.9		15.7
Total energy per cell per pulse	J	38.1		38.7
Total power per cell	kW	1.14		1.16
Core power loss	MW	1.60		4.07
Capacitance charging power	MW	1.03		3.07
Mismatch power	MW	1.52		4.84
Total power	MW	4.16		12.0
Dielectric fluid temp increase	K		10.0	
Flow rate of dielectric fluid	gms/sec-cell	24.8		22.2
Max core temp increase	K	10.7		10.9

Bibliography

[1] P. Wilson, SLAC, Private Communication

[2] W.C. Turner, *An Induction Linac Approach to Phase Rotation of a Muon Bunch in the Production Region of a $\mu^+\mu^-$ Collider*, LBL-38009(1995). Proceedings of the 9th Advanced ICFA Beam Dynamics Workshop, Ed. J.C. Gallardo, AIP Press, to be published.

[3] Allied-Signal, Parsippany, New Jersey.

[4] C.H. Smith, *Applications of Amorphous Magnetic Materials at Very-High Magnetization Rates*, Proc. of Magnetism and Magnetic Materials Conference, Boston (1989).

[5] S. Yu et al., *Relativistic-Klystron Two-Beam Accelerator Based Power Source for a 1 TeV Center-of-Mass Next Linear Collider Preliminary Design Report*, UCRL-ID-119906 (1995).

Collaborators

- H. G. Kirk, (BNL) Editor
- M. Green, (LBNL)
- A. Moretti, (FermiLab)
- W. C. Turner, (LBNL)
- Y. Zhao, (BNL)

List of Figures

List of Tables